Practical frequency-hopping MIMO joint radar communications: Design and experiment

Jiangtao Liu [a], Kai Wu [b], Tao Su [a,*], J. Andrew Zhang [b]

[a] National Key Laboratory of Radar Signal Processing, Xidian University, Xi'an, Shaanxi 710071, China
[b] Global Big Data Technologies Centre, University of Technology Sydney, NSW 2007, Australia

ARTICLE INFO

ABSTRACT

Joint Radar and Communications (JRC) can implement two Radio Frequency (RF) functions using a single of resources, providing significant hardware, power and spectrum savings for wireless systems requiring both functions. Frequency-Hopping (FH) MIMO radar is a popular candidate for JRC because the achieved communication symbol rate can greatly exceed the radar pulse repetition frequency. However, practical transceiver imperfections can cause many existing theoretical designs to fail. In this work, we reveal for the first time the non-trivial impact of hardware imperfections on FH-MIMO JRC and model the impact analytically. We also design new waveforms and correspondingly develop a low-complexity algorithm to jointly estimate the hardware imperfections of unsynchronized receiver. In addition, using low-cost software-defined radios and Commercial Off-The-Shelf (COTS) products, we build the first FH-MIMO JRC experimental platform with simultaneous over-the-air radar and communication validation. Confirmed by simulation and experimental results, the proposed designs achieve high performance for both radar and communications.

1. Introduction

The proliferation of wireless systems has caused severe spectrum congestion and scarcity worldwide. To alleviate this problem, Joint Radar and Communications (JRC) has been identified as a promising solution [1,2]. By sharing waveform, spectrum frequency, hardware and signal processing modules, JRC can significantly improve the cost, energy and spectral efficiency of wireless systems that require both sensing and communications functions [3]. One of the most important JRC designs is radar-centric by integrating data communications into existing radar platforms [4]. Such a design is also referred to as Dual-Function Radar-Communication (DFRC) in the open literature [5].

Initial DFRC works, e.g., [6–8], use the Linear Frequency-Modulated (LFM) signal-based pulsed radars due to their wide applicability in the radar community. In general, these works [6–8] are due to the frequency modulation rate, e.g., positive and negative, to one communication symbol per radar Pulse Repetition Time (PRT). To increase the communication symbol rate, more recent DFRC designs tend to use MIMO radars due to their rich Degree of Freedom (DoF) in waveform design. For example, the beam patterns of a MIMO radar are optimized to take advantage of sidelobes to conduct communication modulations,

e.g. Phase Shift Keying (PSK) and Amplitude Shift Keying (ASK) [9,10]. The MIMO radar waveform has also been optimized to perform unconventional modulations, e.g., code shift keying [11] and waveform shuffling [12]. Although more information bits can be carried per symbol (compared to the original LFM-based DFRC designs), these works [9–12] still embed an information symbol over one or more radar pulses. Thus, the symbol rate they achieve is still limited by the radar Pulse Repetition Frequency (PRF), the reciprocal of PRT.

Recently, Frequency-Hopping (FH) MIMO (FH-MIMO) radar has attracted considerable interest in DFRC designs [4,13–21]. Compared with other pulsed MIMO radars, FH-MIMO radar further divides each pulse into multiple sub-pulses, also called hops, allowing the communication symbol rate to exceed the radar PRF [4]. In addition, FH-MIMO radars also provide new DoFs for information modulation, such as the combinations of hopping frequencies [17] and also the permutations [21].

However, as in single-radio communications, the effective demodulation of FH-MIMO DFRC generally requires accurate channel estimation and transceiver time/frequency synchronization. Communication training for FH-MIMO DFRC is studied by only a few works in the literature. In [18,19], the estimation of the communication channel and the

Sampling Timing Offset (STO) are studied for FH-MIMO DFRC with a single antenna receiver equipped at the communication User End (UE). In [20], the deep fading problem, which can severely degrade the DFRC performance, is identified and solved by introducing a multi-antenna receiver for the UE. Novel waveforms and methods are also developed to estimate the channel and timing offset. Despite the effectiveness of these designs [18–20], they ignored the Carrier Frequency Offset (CFO) and other hardware errors, such as inconsistency of transceiver front-ends.

In this paper, we develop a practical FH-MIMO DFRC scheme by comprehensively addressing all hardware errors, channel estimation, and time and frequency synchronization. Using Software-Defined Radio (SDR) platforms and Commercial Off-The-Shelf (COTS) products, we build an FH-MIMO DFRC experimental platform with both radar and communication functions. In addition, we perform over-the-air outdoor and indoor experiments to validate the effectiveness of the proposed designs and analysis in real-world scenarios. The main contributions and results are summarized as follows.

1. We investigate the effects of practical hardware errors on FH-MIMO DFRC, including STO, CFO and Front-End Errors (FEE). Here, FEE includes the coupled errors from Radio Frequency (RF) chains and antennas at both the radar transmitter and communication receiver sides. We model these errors and demonstrate their non-trivial impact on FH-MIMO DFRC. To the best of our knowledge, this is the first time all these hardware errors are considered together for FH-MIMO DFRC.

2. We design new DFRC waveforms by introducing moderate modifications to conventional FH-MIMO radar waveforms. We also develop a low-complexity algorithm for joint estimation of STO, CFO and FEE at a communication receiver. Moreover, we identify some useful features of the effects of STO, CFO, and FEE under the proposed waveforms and exploit these features to further improve the accuracy of estimating these practical errors.

3. We build the first FH-MIMO DFRC experimental platform based on Xilinx Zynq SDR [22] and ADI's FMCOMMS3 RF board [23]. We also perform the first over-the-air experiments, performing both radar and communications simultaneously. Using the proposed FH-MIMO DFRC waveforms, the radar sensing results are highly consistent with the sensing scenario, as extracted from a high-resolution satellite map. This indicates that the proposed waveform design has a minimal impact on radar sensing. Furthermore, we process the experimental data collected at a communication receiver using the proposed estimation methods. The communication performance achieved is greatly improved over the state of the art, which does not account for all hardware errors as we do.

We emphasize that although our work focuses on FH-MIMO DFRC, the design and analysis have the potential to serve DFRC based on other radar and communication systems. This is because the hardware errors considered in this work, namely STO, CFO and FEE, are common to most, if not all, wireless systems.

We also note that most FH-MIMO DFRC and other radar-based DFRC have been mainly performed through theoretical analysis and simulations. Only a few works have illustrated DFRC through prototypes or proof-of-concept platforms. In [24], the communication function of the FH-MIMO DFRC using differential PSK modulations is implemented using the Universal Software Radio Peripheral (USRP). With a focus on validating the communication feasibility, the work employs a single-antenna transmitter and receiver and makes them synchronized. In contrast, our work considers a more practical case with a widely separated transmitter and receiver that are not physically synchronized. In [25], a prototype is developed to demonstrate a spatial modulation-based DFRC scheme. In [26], a low-complexity proof-of-concept platform called JCR70 was developed for an all-digital joint communications radar at a carrier frequency of 73 GHz and a bandwidth of 2 GHz. These works [25,26] use specially designed hardware for specific DFRC schemes. Despite a lack of generality, they are pioneers in their respective fields. In addition, we note that, since around 2009, there has been a constant interest in using SDR platforms to perform communication waveform-based radar sensing [27–29]. These works provide great guidance in the design of proof-of-concept prototypes based on SDR platforms. However, they mainly focus on using communication waveforms for sensing, while we address a different problem of using radar signals for communication.

The rest of the paper is organized as follows. Section 2 provides the signal model of FH-MIMO DFRC and introduces how information is embedded in the DFRC. Section 3 first illustrates the impact of practical hardware errors on the FH-MIMO DFRC and then develops new waveforms and methods to estimate and remove these errors. Section 4 builds an FH-MIMO DFRC experimental platform and shows simulation and experimental results. Section 5 concludes the paper.

2. Signal model of FH-MIMO DFRC

This section briefly describes the principle of FH-MIMO radar-based DFRC, including how the radar works and how data communication is performed by reusing the radar waveform.

2.1. FH-MIMO radar

The FH-MIMO radar considered here is a pulse-based orthogonal MIMO radar. It uses separate but coherent transceiver arrays to achieve the extended array aperture. It also employs fast frequency hopping; namely, each radar pulse is divided into multiple sub-pulses, i.e., hops, and the frequency changes between hops and antennas. Let B denote the radar bandwidth. The frequency band is divided into K sub-bands. The baseband frequency of the k-th sub-band is $f_k = \frac{\left(\left\lfloor -\frac{K}{2} \right\rfloor + k\right)B}{K}$ ($k = 0, 1, \cdots, K-1$). The baseband frequency of the h-th hop at antenna m is denoted by f_{hm} which can take f_k ($k \in [0, K-1]$). Denote the total number of hops in a radar pulse as H. Then, the signal transmitted by antenna m in a radar pulse can be given by

$$s_m(t) = e^{-j2\pi f_{hm}t}, \ 0 \leq t \leq T + hT, \ h = 0, \cdots, H-1 \qquad (1)$$

where T denotes the time duration of a hop (sub-pulse). To facilitate DFRC, we use the following constraints [14],

$$f_{hm} \neq f_{hm'} \ (m \neq m'), \quad BT/K \in \mathbb{I}_+ \qquad (2)$$

where $\mathbb{I}_+$ denotes the set of positive integers. As a result of the above constraints, the signals transmitted by the M antennas at each hop are orthogonal, i.e., $\int_0^T s_{hm}(t)s_{hm'}^*(t)\mathrm{d}t = 0$ given $m \neq m'$. An FH-MIMO radar receiving processing scheme will be presented in Section 3.4.

2.2. FH-MIMO DFRC

Regarding the DFRC scheme introduced in [18]. The communication information can be transmitted in two ways. *First*, the transmitted signal in each hop and antenna can be multiplied by a PSK symbol, as denoted by $e^{j\varpi_{hm}}$, where $\varpi_{hm} \in \Omega_J$ ($J \geq 1$) and $\Omega_J = \left\{0, \frac{2\pi}{2^J}, \cdots, \frac{2\pi(2^J-1)}{2^J}\right\}$ is a PSK constellation with the modulation order J. *Second*, the combination of the hopping frequencies at each hop is also used to transmit information, which is referred to as Frequency Hopping Code Selection (FHCS) [17]. In particular, given K radar sub-bands and M transmitter antennas, there can be C_K^M numbers of combinations when selecting M out of K sub-bands. FHCS uses these combinations to transmit information bits whose maximum number is $\left\lfloor \log_2(C_K^M) \right\rfloor$, where "$\lfloor \ \rfloor$" rounds the enclosed number towards negative infinity.

For simplicity, we use a single-antenna communication receiver to illustrate information demodulation in FH-MIMO DFRC. Let i be the PRT index and β_{ihm} be the complex channel gain between m-th transmitter antenna of the radar and the communication receiver at i-th PRT.

Where $\upsilon(t)$ denotes AWGN, and M denotes the number of transmit antennas. The communication-received signal at hop h can be given by

$$s_{ih}(t) = \sum_{m=0}^{M-1} \beta_{ihm} e^{j\varpi_{ihm}} e^{-j2\pi\Delta f_{ihm}t} + \upsilon(t) \tag{3}$$

To demodulate information symbols, we need to estimate f_{ihm} and ϖ_{ihm}. Given the constraint (2), the former can be estimated by detecting the strongest M peaks in the Fourier transform of $y_{ih}(t)$. In contrast, ϖ_{ihm} is more difficult to estimate, because we need to know β_{ihm} first. Their estimation is studied in [18] under the ideal condition of no time or frequency offset between the radar transmitter and communication receiver. In [19], the timing offset is considered, not the frequency offset. Furthermore, the array calibration error has not been considered for FH-MIMO DFRC. These non-ideal conditions will be investigated in the following.

3. Practical FH-MIMO DFRC design

In this section, we first investigate the impact of practical transceiver errors on FH-MIMO DFRC. Then we design waveforms and propose novel methods to estimate and remove the errors.

3.1. Impact of practical transceiver errors

Clock asynchrony between the radar transmitter and a communication receiver can cause STO and CFO. Define $\Delta\omega = 2\pi\Delta f_c$, where f_c denotes the carrier frequency. It changes slowly with time and can be treated as a fixed value here. Unlike the CFO, the STO accumulates, and its impact varies rapidly with time. Let Δt_0 denote the initial STO and ΔT_s be the sampling time difference between the radar transmitter and the communication. Then, at the h-hop of the i-th PRT, the accumulated STO is given by

$$\Delta t_{ih} = \Delta t_0 + (iN_p + hN_h)\Delta T_s \tag{4}$$

where N_p (N_h) is the number of samples in one PRT (hop). Based on (3), the communication received signal in the h-th hop and i-th PRT, including CFO and STO, can be expressed as

$$s_{ih}(t) = \sum_{m=0}^{M-1} \beta_{ihm}(\omega_{ihm})\mathrm{rect}\left(\frac{t - iT_p - hT}{T}\right) \times$$
$$e^{j(\omega_{ihm}+\Delta\omega)(t+\Delta t_{ih})}e^{j\varpi_{ihm}} \tag{5}$$

where the $\mathrm{rect}(\frac{x}{T})$ is the rectangular function that takes one for $x \in [0, T]$ and zero elsewhere. Here, T_p and T denote the time of a PRT and a hop, respectively. Also, $\beta_{ihm}(\omega_{ihm})$ is a function of ω_{ihm}, where $\omega_{ihm} = 2\pi f_{ihm}$. Note that $\beta_{ihm}(\omega_{ihm})$ takes into account other frequency-dependent gains caused by the radio frequency chains of different antennas.

Calculating the Fourier transform of $s_{ihm}(t)$ at $\omega = \omega_{ihm}$, we obtain

$$S_{ihm} \overset{(a)}{=} \int_0^T s_{ihm}(\tilde{t})e^{-j\omega_{ihm}(\tilde{t}+iT_p+hT)}d\tilde{t} \overset{(b)}{\approx} \int_0^T \beta_{ihm}(\omega_{ihm})$$
$$e^{j(\omega_{ihm}+\Delta\omega)(\tilde{t}+iT_p+hT+\Delta t_{ih})}e^{j\varpi_{ihm}}e^{-j\omega_{ihm}(\tilde{t}+iT_p+hT)}d\tilde{t}$$
$$\overset{(c)}{\approx} \mathcal{A}(\Delta\omega)\beta_{ihm}(\omega_{ihm})e^{j\varpi_{ihm}}e^{j\omega_{ihm}\left(\Delta t_0+(iN_p+hN_h)\Delta T_s\right)} \times$$
$$e^{j\Delta\omega(iT_p+hT)}e^{j\Delta\omega(iN_p+hN_h)\Delta T_s} \tag{6}$$

where the substitution $\tilde{t} = t - iT_p - hT$ is performed to get $\overset{(a)}{=}$ with the integral variable changed from t to $\tilde{t}$; the expression of $s_{ihm}(t)$ given in (5) is plugged in $\overset{(a)}{=}$ to get $\overset{(b)}{\approx}$; and $\overset{(c)}{\approx}$ is obtained by replacing Δt_{ih} with its expression given in (4) and by taking $e^{j\Delta\omega\Delta t_0} \approx 1$. Note that the integral over $\tilde{t}$ yields

$$\mathcal{A}(\Delta\omega) = T\sin\frac{\Delta\omega T}{2} \Big/ \left(\frac{\Delta\omega T}{2}\right)e^{j\frac{\Delta\omega T}{2}} \tag{7}$$

Moreover, the approximation $\overset{(b)}{\approx}$ is because we have neglected the Fourier transforms of the signals from other antennas.

It is clear from (6) that STO, represented by Δt_{ih} and CFO, as represented by $\Delta\omega$, have non-trivial effects on the communication demodulation. To estimate the PSK symbol ϖ_{ihm}, all the other phases must first be estimated and suppressed. This will be investigated next. In particular, we develop the demodulation methods, introducing some conditions on the waveform to enable the new methods. We then translate these conditions into waveform design.

3.2. Proposed demodulation method

From (6), we obtain the following, when $\omega_{ihm} = 0$ and $\varpi_{ihm} = 0$,

$$\tilde{S}_{ihm} = S_{ihm}|_{\omega_{ihm}=0} = \mathcal{A}(\Delta\omega)\beta_{ihm}(0)\times$$
$$e^{j\Delta\omega(iT_p+hT)}e^{j\Delta\omega(iN_p+hN_h)\Delta T_s} \tag{8}$$

Note that i, h and m are indexes of PRT, hop and antennas, respectively. The result in (8) facilitates the estimation of $\Delta\omega$, as detailed below.

First, similar to $\tilde{S}_{ihm}$, we can set $\omega_{(i+1)hm} = 0$ and obtain

$$\tilde{S}_{(i+1)hm} = S_{(i+1)hm}|_{\omega_{(i+1)hm}=0} = \mathcal{A}(\Delta\omega)\beta_{(i+1)hm}(0)\times$$
$$e^{j\Delta\omega((i+1)T_p+hT)}e^{j\Delta\omega((i+1)N_p+hN_h)\Delta T_s} \tag{9}$$

Then, taking the ratio between $\tilde{S}_{(i+1)hm}$ and $\tilde{S}_{ihm}$ leads to

$$\frac{\tilde{S}_{(i+1)hm}}{\tilde{S}_{ihm}} = \frac{\beta_{(i+1)hm}(0)}{\beta_{ihm}(0)}e^{j\Delta\omega(T_p+N_p\Delta T_s)} \approx e^{j\Delta\omega T_p} \tag{10}$$

where the approximation is because $|\Delta\omega N_p\Delta T_s| \ll \frac{2\pi}{2^J}$ and $\beta_{ihm}(0) \approx \beta_{(i+1)hm}(0)$. The validity of the first condition is illustrated in Appendix A. For the second, because the channel is approximately unchanged in a single PRT with a short duration, e.g., 40 μs to be validated in our experiment. From (10), we can estimate CFO as

$$\widehat{\Delta\omega} = \arg\left\{\frac{\tilde{S}_{(i+1)hm}}{\tilde{S}_{ihm}}\right\} \Big/ T_p \tag{11}$$

Note that $\Delta\omega$ and ω are the same multiples of Δf_{CLK} and f_{CLK}, respectively. Here, Δf_{CLK} denotes the clock offset and f_{CLK} is the nominal clock frequency. The ratio between $\Delta f_{\mathrm{CLK}}/f_{\mathrm{CLK}}$ is often called clock stability. Therefore, with $\widehat{\Delta\omega}$ attained, we can estimate the clock stability, as given by

$$\hat{\rho} = \widehat{\Delta\omega}/\omega \tag{12}$$

where ω denotes the nominal local oscillator angular frequency. Based Appendix A, we can further estimate STO ΔT_s as

$$\widehat{\Delta T_s} = -\hat{\rho}\Big/\left(f_s^{(t)}(1-\hat{\rho})\right) \tag{13}$$

where $f_s^{(t)}$ is the sampling frequency at the transmitter. When ΔT_s is estimated, we see from (4) that Δt_{ih} is also partially estimated.

From (6), we see that the remaining unknowns that affect the communication demodulation, i.e., the estimation of ϖ_{ihm}, is $\beta_{ihm}(\omega_{ihm})e^{j\omega_{ihm}\Delta t_0}$. The coupling of the two terms makes their individual estimates difficult to obtain. Therefore, we consider their joint estimation. To do so, we introduce $\check{S}_{i_1h_1m}$ ($h_1 \neq h$) which is obtained by taking $\varpi_{i_1h_1m} = 0$ and $\omega_{i_1h_1m} = 2\pi kB/K$ in (6), where B is the signal bandwidth. Unlike $\tilde{S}_{ihm}$ given in (8) with the zero hopping frequency, $\check{S}_{i_1h_1m}$ is obtained under non-zero hopping frequency. Furthermore, they can be obtained under the same PRT with $i_1 = i$, but they are always obtained in different hops, i.e., $h_1 \neq h$.

Assuming that the above conditions are satisfied, we consider the ratio between $\check{S}_{i_1h_1m}$ and $\tilde{S}_{i_1hm}$, where the latter is obtained by taking $i = i_1$ in (8). This ratio can be expressed as

$$d_{mk} = \frac{\check{S}_{i_1 h_1 m}}{\tilde{S}_{i_1 hm}} = C \frac{\beta_{i_1 h_1 m}\left(\frac{2\pi k}{K}\right)}{\beta_{i_1 hm}(0)} e^{j\frac{2\pi k \Delta t_0}{K}}, \quad k = 1, \cdots, K-1 \tag{14}$$

$$\text{s.t. } C = e^{j\frac{2\pi k(i_1 N_p + h_1 N_h)\Delta T_s}{K}} e^{j\Delta\omega(h_1 - h)T} e^{j\Delta\omega(h_1 - h)N_h \Delta T_s}$$

Similarly, let us further construct the ratio between $\check{S}_{i_2 h_2 m}$ and $\tilde{S}_{i_2 hm}$ with $i_2 \neq i_1$ and $h_2 \neq h$. After some basic calculations, we obtain

$$\frac{\check{S}_{i_2 h_2 m}}{\tilde{S}_{i_2 hm}} = d'_k \mathcal{D} e^{j\varpi_{i_2 h_2 m}}, \quad \text{s.t. } d'_k = C \frac{\beta_{i_2 h_2 m}\left(\frac{2\pi k}{K}\right)}{\beta_{i_2 hm}(0)} e^{j\frac{2\pi k \Delta t_0}{K}},$$

$$\mathcal{D} = e^{j\frac{2\pi k\left((i_2 - i_1)N_p + (h_2 - h_1)N_h\right)\Delta T_s}{K}} e^{j\Delta\omega(h_2 - h_1)T} \times$$

$$e^{j\Delta\omega(h_2 - h_1)N_h \Delta T_s} \tag{15}$$

where C is given in (14), and h_1 in $\mathcal{D}$ is due to the inclusion of C in d'_k. Note that $\mathcal{D}$ can be estimated based on the estimates obtained in (11) and (13). Assuming that d'_k is known for the moment, then we can estimate $\varpi_{i_2 h_2 m}$ as

$$\widehat{\varpi}_{i_2 h_2 m} = \arg\left\{\frac{\check{S}_{i_2 h_2 m}}{d'_k \mathcal{D} \tilde{S}_{i_2 hm}}\right\} \quad \text{s.t. } \omega_{i_2 h_2 m} = 2\pi k B/K \tag{16}$$

Our next question is how to know d'_k. Comparing (14) and (15), we can see that d'_k has a very similar form to d_{mk}. In fact, they are approximately the same, as ensured by the following lemma.

Remark 1. Provided that $|(i_1 - i_2)T_p|$ is less than the stable time of the transceiver front-ends, we have $d'_k = d_{mk}$, where T_p is the PRT duration. From (14) and (15), we can see that d'_k and d_{mk} are almost the same, except for some differences in the subscripts of the $\beta.(\cdot)$ terms. As shown in the text below (5), $\beta.(\cdot)$ is the composite effect of the channel response and the complex gains of the transceiver front-ends. In the same radar pulse, the channel response is fixed. Therefore, the two ratios $\frac{\beta_{i_1 h_1 m}\left(\frac{2\pi k}{K}\right)}{\beta_{i_1 hm}(0)}$ and $\frac{\beta_{i_2 h_2 m}\left(\frac{2\pi k}{K}\right)}{\beta_{i_2 hm}(0)}$ are only dependent on the complex gains of the transceiver front-ends. As a result, the ratios are the same if i_1 and i_2 satisfy the condition stated in the lemma. We note that in modern transceivers, front-ends are generally stable in a continuous operation, i.e., a whole course of running after a system is powered on. This is also validated through our experiments, which will be presented in Section 4.3.

3.3. Novel DFRC waveform designs

We have shown above that under certain conditions imposed on FH-MIMO waveforms, we can suppress unknown channel and hardware errors to estimate communication symbols. These conditions can be ensured by proper waveform design, as shown below.

From (8) to (13), we can see the importance of the zero baseband frequency, i.e., $k = 0$ for some ω_{ihm}. Since different antennas will have different channel responses and front-end gains, we need to ensure that each antenna takes the zero baseband frequency at least once. Achieving this requires at least M hops, since different hopping frequencies are used for different antennas in the same hop, as shown in (2). Thus, our first waveform design can be written as

Design 1 (D1): $\omega_{ihm} = 0$ and $\varpi_{ihm} = 0$ at $h = m$.

For Remark 1, we know that d_{mk} must be computed to estimate d'_k. From (14), we can see that d_{mk} is obtained under $\omega_{ihm} = 2\pi k B/K$ and $\varpi_{ihm} = 0$. Therefore, to avoid greatly of the original radar waveform, we adopt the following waveform design to calculate d_{mk} ($k = 0, 1, \cdots, K-1$) over K different PRTs:

Design 2 (D2): $\omega_{ihm} = 2\pi \langle i \rangle_K B/K$ and $\varpi_{ihm} = 0$ at $h = m + 1$, given $H \geq M + 1$, where $\langle i \rangle_K$ denotes the modulo-K of i.

Note that $h = m + 1$ is because $h = m$ was used in Design 1.

Algorithm 1 Proposed FH-MIMO DFRC Scheme.

Input: M (radar transmitter antenna number), H (the number of hops in a radar pulse), T (hop duration), T_p (PRT duration), K (the number of sub-bands), B (radar bandwidth), $s_{ih}(t)$ given in (5) (the time-domain communication-received signal)

1. For each i in $S_x = \{0, 1, \cdots, K-1\}$:
   (a) Take the Fourier transform of $s_{ih}(t)$ given in (5);
   (b) Identify the largest M peaks, yielding S_{ihm} given in (6);
   (c) For each m in $1, \cdots, M$, calculate d_{mk} given in (14) by taking $i_1 = i$, $h_1 = m + 1$ (due to (D2)) and $h = m$ (due to (D1));
   (d) For each h_2 and m, calculate $\frac{\check{S}_{i_2 h_2 m}}{\tilde{S}_{i_2 hm}}$ in (15) by taking $i_2 = i$ and $h = m$ (due to (D1));
2. Estimate $\widehat{\Delta\omega}$ as in (11), where $h = m$ based on (D1);
3. Estimate $\widehat{\Delta T_s}$ jointly using (12) and (13);
4. For S_x, $h \neq m$ or $(m+1)$:
   (a) If $\omega_{ihm} = 2\pi k B/K$, set $i_1 = k$, $h_1 = m + 1$, $i_2 = i$ and $h_2 = h$;
   (b) Estimate $\mathcal{D}$ based on (15);
   (c) Estimate ϖ_{ihm} based on (16) with $h = m$ taken for $\tilde{S}_{i_2 hm}$ in the denominator;

The two designs are sufficient for effective communication demodulation in a practical FH-MIMO DFRC with hardware errors and unknown channels. For clarity, we summarize the entire procedure in Algorithm 1. While most of the steps in Algorithm 1 are straightforward based on the illustrations in this section, we provide additional notes on several important steps. For brevity, we include only K PRTs in Step 1). However, we note that each successive K PRTs will be used together for communication demodulation. The main reason is that (D2) only allows us to estimate one d_{mk} per PRT. While this design is unnecessary, it introduces minimal changes to the primary radar function. In Step 1b), identifying M peaks from the Fourier transform result is not complicated; however, assigning the peaks to the M radar transmitter antennas is. Therefore, we use another waveform constraint [19].

$$\omega_{ihm} < \omega_{ihm'}, \quad m' > m \tag{17}$$

To implement the constraint, we let the FH-MIMO randomly select its hopping frequencies, then reorder them in ascending order and assign them to the antennas, one at a time. A nice feature was discovered in [18], which states that the above reordering does not change the range ambiguity function of the underlying FH-MIMO radar. In Step 2) of Algorithm 1, the estimates $\widehat{\Delta\omega}$ obtained under different i's can be averaged to improve the estimation performance. Then Step 3) can be performed based on the improved $\widehat{\Delta\omega}$ to obtain a more accurate $\widehat{\Delta T_s}$.

We remark that the FH-MIMO DFRC design is radar-centric in this work; namely, we seek to introduce only minimal changes to the radar yet facilitate effective communications in the presence of hardware errors. The waveform design shown above requires only a few hops over antennas to use the assigned hopping frequencies as opposed to the random selection in the original radar. Thus, we expect the introduced waveform design to have little impact on the radar function. This will be validated in Section 4. The significance of our design to communications is that for the first time, the practical hardware errors are, modeled and effectively suppressed for FH-MIMO DFRC. Without accounting for these unavoidable practical errors, the communication performance in practice can be relatively poor; this is demonstrated in Section 4 through over-the-air experiments.

Note that the complexity of Algorithm 1 is quite low, as only Fourier transform and some elementary operations are required (as opposed to computationally intensive matrix operations). Based on the algorithm, the complexity of Step 1 is in the order of $\mathcal{O}(KHT f_s \log_2(T f_s))$, where the fast Fourier transform is used to compute the DFT in Step 1a), $T f_s$ is the size of the FFT, and KH is the number of FFTs performed for a complete run of Algorithm 1. Step 2 or 3 has a $\mathcal{O}(K)$ complexity. In addition, Step 4 has a $\mathcal{O}(3MK)$ complexity. Thus, the total complexity of Algorithm 1 is dominated by Step 1.

3.4. FH-MIMO radar receiving processing

Here is a brief description of an FH-MIMO radar processing scheme. It will be implemented in simulations and experiments. Let $\mathbf{s}_i(t) = [s_{i1}(t), s_{i2}(t), \cdots, s_{iM}(t)]^{\mathrm{T}}$ collect the signals transmitted by the M antennas in the i-th PRT, where $s_{im}(t)$ is obtained by replacing $2\pi f_{hm}$ in (1) by ω_{ihm} designed in Section 3.3. Also, let $\mathbf{y}_i(t) = [y_{i1}(t), y_{i2}(t), \cdots, y_{iN}(t)]^{\mathrm{T}}$ denote the signals received by the N receiver antennas. Denote the steering vectors of the transmitter and receiver arrays by $\mathbf{a}_t(\theta)$ and $\mathbf{a}_r(\theta)$, respectively. Since they are co-located, they have the same direction. Considering a single target for simplicity, the radar echo signal at the i-th PRT can be given by

$$\mathbf{y}_i(t) = \delta \mathbf{a}_r(\theta)\mathbf{a}_t^{\mathrm{T}}(\theta)\mathbf{s}_i(t-\tau) + \mathbf{w}_i(t),$$

s.t. $t \in (i-1)T_{\mathrm{PRT}} + [HT, T_{\mathrm{PRT}}]$　　　　　(18)

where τ represents the target echo delay, δ denotes the target scattering coefficient, $\mathbf{w}_i(t)$ collects additive white Gaussian noises (AWGNs), and T_{PRT} is the time duration of a PRT. As mentioned earlier, the FH-MIMO of interest is a pulsed radar. Therefore, there should be no valid echo signal during the radar transmission because the receiver is either turned off or saturated with invalid echo signals. This explains the starting time of each PRT given in (18). The typical steps of radar-receiving processing, as performed in simulations and experiments, are described below.

Matched filtering is a typical first step of pulsed radar signal processing [30]. The filter coefficients are $s_{im}^*(-t)$ ($m = 0, 1, \cdots, M-1$), where "$()^*$" takes conjugate. Since each antenna receives a combination of all transmitted signals, $y_{in}(t)$ must pass through each of the M filters, where $y_{in}(t)$ denotes the n-th entry of $\mathbf{y}_i(t)$ given in (18). The matched filtering result can be written as

$$\tilde{y}_{ip}(t) = y_{in}(t) \circledast s_m^*(-t), \; p = (n-1)M + m \quad (19)$$

where $\circledast$ calculates the linear convolution.

Moving target detection (MTD) is often performed after the matched filter. For $\tilde{y}_{ip}(t)$, a Fourier transform can be performed over i, leading to the so-called Range-Doppler Map (RDM),

$$\tilde{Y}_{fp}(t) = \sum_{i=0}^{I-1} \tilde{y}_{ip}(t)e^{-j2\pi fiT_{\mathrm{PRT}}} \quad (20)$$

where f and t span the Doppler and range dimensions, respectively.

Target detection can be performed based on $\sum_{p=0}^{P-1} |\tilde{Y}_{fp}(t)|$, where the incoherent accumulation over p (indexing spatial channels) is performed, since we do not have the angular information yet. Otherwise, coherent beamforming can be performed. The Constant False Alarm Rate (CFAR) detector has been widely used for target detection and will be used for our simulation and experiment. Interested readers are referred to [30] for the details of the CFAR detector. An intuitive simulation tutorial is also available at [31]. Let (f^*, t^*) denote the location of a target. By extracting the signal at each RDM, we obtain

$$\mathbf{z} = \left[\tilde{Y}_{f^*0}(t^*), \tilde{Y}_{f^*1}(t^*), \cdots, \tilde{Y}_{f^*(P-1)}(t^*)\right]^{\mathrm{T}} \quad (21)$$

where $P = MN$ according to (19).

Angle estimation is performed using $\mathbf{z}$. Based on (18), the steering vector representing the spatial information in $\mathbf{z}$ can be written as $\tilde{\mathbf{a}}(\theta) = \mathbf{a}_r(\theta) \otimes \mathbf{a}_t(\theta)$, where $\otimes$ denote the Kronecker product. In practice, the radio frequency chains associated with transmitter and receiver antennas always present some differences. Let $\mathbf{e}_t$ and $\mathbf{e}_r$ denote the relative differences between different channels on the transmitter and receiver sides, respectively. Taking them into account, the steering vector can be
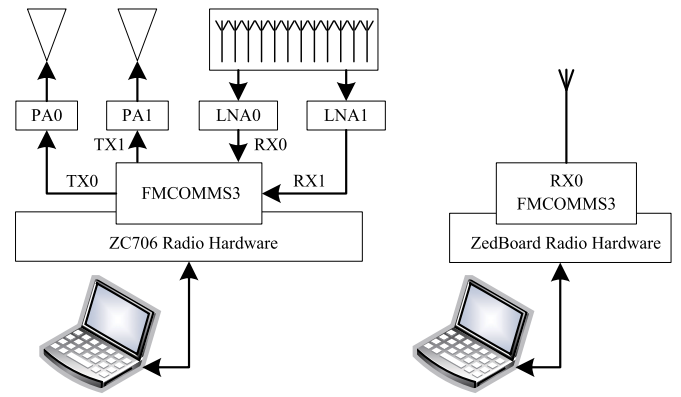
Fig. 1. The schematic diagram of the testing system.

rewritten as $\breve{\mathbf{a}}(\theta) = \tilde{\mathbf{a}}(\theta) \odot (\mathbf{e}_r \otimes \mathbf{e}_t)$, where $\odot$ denotes the element-wise multiplication. Therefore, a naive angle estimate can be obtained as[1]

$$\hat{\theta} = \mathrm{argmax}_{\theta_l=2\pi l/L} \; |\breve{\mathbf{a}}(\theta_l)^{\mathrm{H}}\mathbf{z}|^2, \; l = 0, 1, \cdots, L-1 \quad (22)$$

where L can be a relatively large value for a fine spatial resolution. Note that L is the number of angle grids, and $\mathbf{z}$ is an array snapshot formulated at a fixed time slot t^*, as shown in (21). Therefore, increasing L does not increase the observation time.

4. Over-the-air FH-MIMO DFRC experiments

In this section, we perform over-the-air experiments to validate the proposed FH-MIMO DFRC scheme. As shown in Fig. 1, we use two SDR platforms, one for radar transceiving and the other for communication receiving. For the radar system, the two transmit RF chains of the SDR platforms are connected to two horn antennas through two power amplifiers. The two receive RF chains on the same SDR are used for radar receiving. To facilitate high angular resolution, we adopt a 12-antenna linear array for radar receiving. For the communication receiver, only one RF chain on the SDR platform is used along with an omnidirectional antenna. Next, we describe the radar and communication experimental platforms in more detail.

4.1. Schematic diagram and experiment platform

The schematic diagram of our testing system is shown in Fig. 1. We use the Xilinx Zynq software-defined radio (SDR) ZC706 [34] and Zed-Board [35] to build the FH-MIMO radar and communication receiver, respectively. Both SDRs are equipped with RF FPGA mezzanine card (RF FMC) boards, specifically FMCOMMS3 [23]. Each FMCOMMS3 supports two transmitting and two receiving RF chains with the RF range of 70 MHz ~ 6 GHz and a baseband frequency range of 200 KHz ~ 56 MHz. FMCOMMS3 uses a 40 MHz oscillator with the 10 ppm stability [36]. Note that both SDRs are supported by MATLAB [22]. Thus, they are connected to host computers, where MATLAB is installed and used to program and control the SDRs independently.

For the FH-MIMO radar, we use MATLAB to generate the base-band signals of the two transmitting antennas for a CPI and download them once to the ZC706 via. The SDR is configured to transmit the signals cyclically. The two radar receiving channels are configured to capture echo signals in a consecutive time of 204.8 ms, which is equivalent to 8,192,000 samples. Note also that the maximum number of samples that can be transferred in one capture is 8,388,608, a limitation of the

---

[1] More advancing methods, such as the multiple signal classification (MUSIC) [32] and the DFT interpolation-based methods [33], can be employed for more accurate angle estimation.
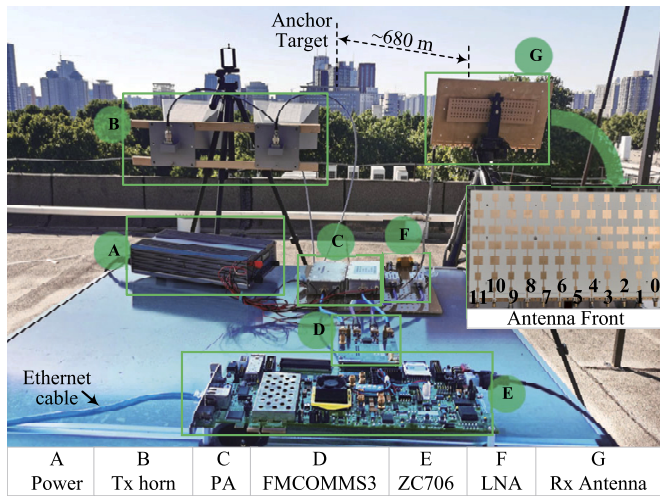
Fig. 2. The established FH-MIMO radar, where the host computer is not shown but connected with the SDR through an Ethernet cable.

Table 1
Parameters of the Established FH-MIMO Radar.

Variable	Parameter	Value
-	Central frequency	5.5 GHz
-	power amplifier gain	43 dB
M	Number of horn antennas	2
-	horn antenna gain	20.39 dB
-	horizontal beamwidth of horn antenna	16°
-	vertical beamwidth of horn antenna	15.5°
-	Maximum transmit power of PA	20 W
N	Number of radar receiver antennas	12
-	Receiving antenna element gain	13 dB
-	Horizontal beamwidth of microstrip antenna	120°
-	Vertical beamwidth of microstrip antenna	20°
-	Low noise amplifier gain	23 dB

used SDR [22]. Note that the echo capture must be triggered in MAT-LAB on the host computer. The communication receiver, as configured similarly to the radar receiver, also needs a triggering signal from the MATLAB connected to the SDR. The radar and communication subsystems are discussed in more detail below.

4.1.1. Radar subsystem

Based on the ZC706, we build a FH-MIMO radar platform, as shown in Fig. 2. A host computer (not shown in the figure) is connected to the SDR through an Ethernet cable (shown on the lower left side). The RF board, FMCOMMS3, is underpinned by an AD9361, which has the maximum output power of 6.5 dBm at 5.5 GHz [37], where 5.5 GHz is the carrier frequency used in our experiments. In addition, we use external Power Amplifiers (PAs) to increase the transmit power of the radar. The maximum output power of the employed PA is 20 W, i.e., 43 dBm. By controlling the output power of AD9361, the transmission power is fixed at 2 W in the sequential experiments. Two identical horn antennas are also used for radar transmission, each connected to an RF chain. A microstrip uniform linear array of 12 antennas is used for radar reception. The antenna spacing is half the wavelength at the center frequency of 5.5 GHz. Two Low-Noise Amplifiers (LNAs) are used, one for each receiving RF chain on FMCOMMS3. Key Parameters of the above components are listed in Table 1.

Here are a few notes. *First*, the AD9361 has an adjustable gain of $-89.75 \sim 0$ dB for the transmitting RF chain and $0 \sim 61$ dB for receiving RF chain. Thus, together with the gains from other components, see Table 1, the maximum transmitting and receiving power gain of the FH-MIMO radar built in Fig. 2 can be $43 (= 0 + 43)$ dB and $84 (= 23 + 61)$ dB, respectively. *Second*, in the experiments, we place the two horn an-
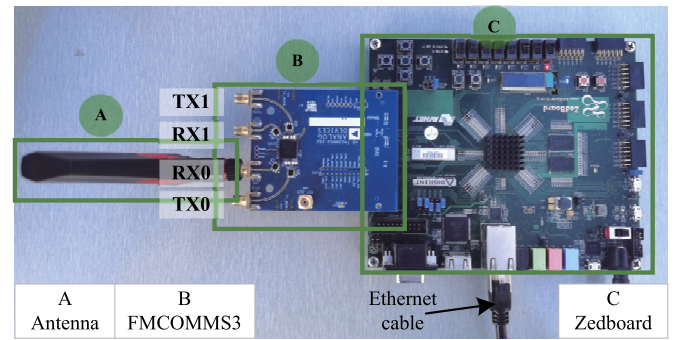
Fig. 3. The Communication Subsystem.

Table 2
Parameters of the FH-MIMO Radar.

Variable	Parameter	Value
B	the Signal Bandwidth	20 MHz
f_k	radar sub-band baseband frequency	$-10 : 1 : 9$ MHz
T	hop duration	1 μs
H	number of hops per pulse	5
T_p	PRT	40 μs
N_c	number of PRTs per CPI	128
f_s	sampling frequency	40 MHz
N_p	number of samples per PRT	$1600(= f_s T_p)$

tennas 6λ apart. According to the MIMO radar processing shown in Section 3.4, how a virtual array of $2 \times 12 = 24$ antennas. *Third*, limited by the number of receiving RF chains on FMCOMMS3, the Time Division Multiplexing (TDM) MIMO is employed to achieve the above-mentioned virtual array. As shown in Fig. 2, the receiving antenna array has 12 elements, each connected to an SMA port. However, as shown in Fig. 3, only two receiving RF chains are received. Therefore, we collect the echo signals from the 12 antennas in six consecutive data captures. In the n-th $(n = 0, 1, \cdots, 5)$ capture, the two receiving SMAs are connected to the n-th and $(n + 6)$-th antenna element shown in Fig. 2. Interested readers are referred to [38] for more details on TDM-MIMO radars.

Based on the hardware features presented in Section 4.1, we set the parameters of the FH-MIMO radar, as shown in Table 2. Since the considered FH-MIMO radar is a pulsed radar, the receiver channel suffers from strong self-interference when the transmitter works. Leading to a blind zone of $cHT/2$ (in meters), where c denotes the microwave speed, T is a hop duration, and H is the number of hops. Given the limited link budget, see Table 1, the maximum measurable distance of the radar platform would be very limited. Therefore, we want to keep the blind zone as small as possible. We set $T = 1$ μs and $H = 5$ to do so. This results in a blind zone of 750 m. Other parameters in Table 2 are straightforward based on the descriptions therein.

4.1.2. Communications subsystem

It is based on the SDR Zed-Board, FMCOMMS3 and an 8 dBi omni-directional antenna, as shown in Fig. 3. Since only downlink communication is considered in this work, the communication subsystem only receives, which is much simpler than the radar system. We do not use an external LNA for the communication subsystem. Therefore, its receiving power gain ranges in $0 \sim 61$ dB, depending only on the AD9361 of FMCOMMS3.

Based on the parameters listed in Table 2, we can calculate the data rate of the radar-enabled communications. As illustrated in Section 2.2, the combinations of hopping frequencies are used as communication data symbols. Given $K = 20$ sub-bands and $M = 2$ transmitting antennas, we have $C_{20}^2 = 190$. Considering the integer number of bits, out of 190 combinations, 128 numbers of combinations can be used to convey 7 bits per radar hop. Given $H = 5$, a total of $7 \times 5 = 35$ bits can be trans-

mitted per PRT using the combinations. Moreover, PSK is also used for information demodulation, one symbol per hop and antenna. Therefore, for an x-bit PSK modulation, the total number of information bits per PRF is xMH.

In each pulse, we have two types of hops. The first type of hops consists of two antennas that use fixed hopping frequencies per D1 and D2, respectively, for training purposes. Consequently, the corresponding hops reduce available frequency points by 2, i.e., $M - 2$. Let the number of hops in this category be denoted by H_D, and its specific value depends on the number of antennas, M. The second type of hops is not constrained to the constraints in D1 or D2, allowing the utilization of the full number of frequency points, K. The number of hops in this category is denoted as $H - H_D$. With trivial details suppressed, the communication data rate can be given by

$$\text{data\_rate} = \underbrace{\left\{ \left[\lfloor \log_2(C_{K-2}^{M-2}) \rfloor + x(M-2) \right] H_D \right\}}_{D1 \text{ and } D2 \text{ hops}}$$
$$+ \underbrace{(\lfloor \log_2(C_K^M) \rfloor + xM)(H - H_D)}_{other \text{ hops}}, \quad H > M \geq 2 \quad (23)$$

For example, let us consider that there will be two hops in each pulse used to estimate the channel parameters, and $M = 2 = H_D, K = 20, H = 5$, for $x = 1, 2, 3$ and 4, the effective communication data rate is $0.675, 0.825, 0.975$, and 1.125 Mbps, respectively.

4.2. Simulation analysis

Before performing experiments, simulations are carried out to validate the proposed FH-MIMO DFRC.[2] We start with validating the radar performance, where the radar is configured as per Table 2. As for the sensing scenario, we set up 50 targets with random speeds, distances and angles that are uniformly distributed in $[-170, 170]$ m/s, $[750, 4, 185]$ m and $[-4, 4]$ deg, respectively. To evaluate the Root Mean Squared Error (RMSE) of the parameter estimations, we perform 100 independent trials, with target parameters randomly generated across trials. For each trial, we perform the radar processing shown in Section 3.4 for target detection and estimation. Both the conventional FH-MIMO radar in Section 2.1 and the radar modified for DFRC in Section 3.3 are simulated for a comparison. In each trial, we generate random bit sequences over PRTs. Specifically, in each PRT, we generate $(7 + xM)(H - 2)$ number of random bits according to (23), where M denotes the number of antennas, H denotes the number of hops per PRT, and x is the number of bits per PSK symbol. Since the first two hops are reserved for channel and transceiver error estimation, the information bits are only carried by the later $(H - 2)$ hops per PRT. Each $(7 + xM)$ bits are mapped to symbols per hop over M antennas. The first 7 bits are used to select the combination of hopping frequencies over antennas. Then, the remaining xM bits are mapped to M numbers of PSK symbols, one for each antenna.

Fig. 4 shows a snapshot of a Range-Doppler Map (RDM) obtained in a single trial. We can see many strong points scattered across the range-Doppler domain, each point representing a target. As shown in Section 3.4, CFAR is performed based on an RDM. The delay and Doppler bins of the detected targets are then used to estimate their parameters. Fig. 5 plots the RMSEs of angle, distance and velocity averaged over all targets and trials. We see that the RMSEs of all parameter estimates first decrease and then converge as the SNR increases. This is consistent with general understanding, and the convergence is due to the quantized distance, velocity and angle grids used during the estimation; see Section 3.4. More importantly, we can see from Fig. 5 that the traditional and new FH-MIMO radar waveforms lead to almost the same
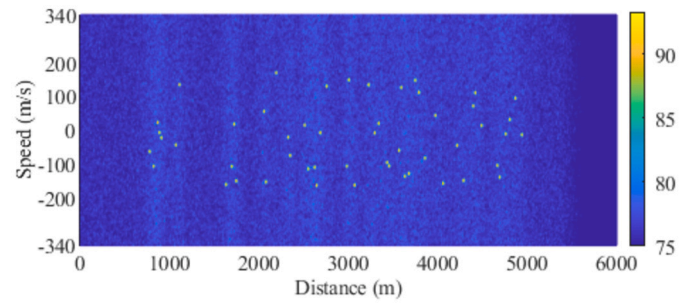
Fig. 4. The 50 random targets for simulation.
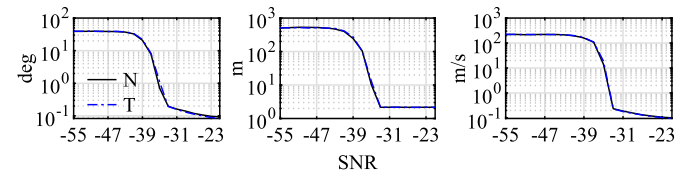
Fig. 5. Root mean squared error (RMSE) of angle, distance and velocity estimations under different SNR, where "N" and "T" represent new and traditional FH-MIMO radar waveforms, respectively. Note that the SNR in the x-axis is for the raw echo signal, i.e., without any processing gain, at the radar receiver.
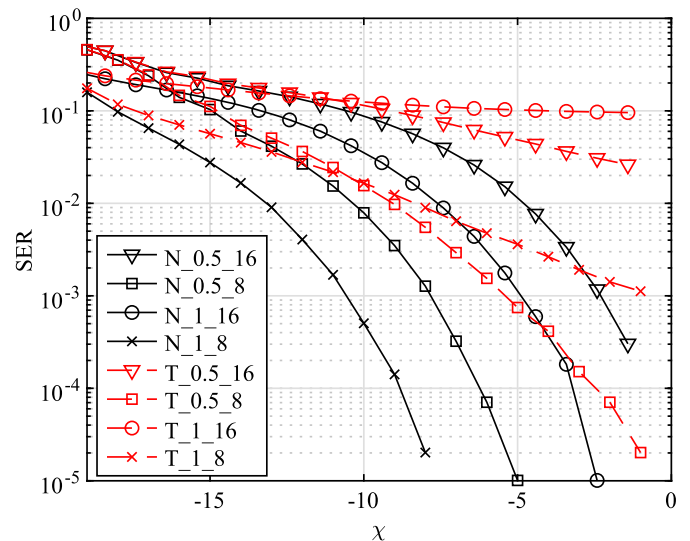
Fig. 6. Simulated SER versus χ, where χ is the difference between SNR and the number of bits per symbol in decibels. In the legend, 'N' denotes 'the proposed new method', while 'T' represents the 'traditional method' [19]; 0.5 and 1 are different hop duration in milliseconds; and 8 and 16 are the modulation orders of PSK symbols. Note that the SNR at the communication receiver is independent of the SNR at the radar receiver, i.e., that shown in the x-axis of Fig. 5.

estimation performance. This validates that the proposed waveform designs for DFRC only incur minimal changes to the underlying FH-MIMO radar.

Next, we demonstrate the communication performance of FH-MIMO DFRC using the Symbol Error Rate (SER) metric. FHCS and PSK, are simulated as shown in Section 2.2. Most of the radar configurations in Table 2 are used. However, we also consider two different hop durations, i.e., 0.5 μs and 1 μs. As for the PSK, we simulate 8PSK and 16PSK. In this simulation, we let the communication receiver know the channel responses. Thus, the results here provide a performance lower bound of the experimental results to be presented shortly.

Fig. 6 compares the SER performance of the benchmark method (as indicated by 'T' in the figure) and the proposed method (as indi-
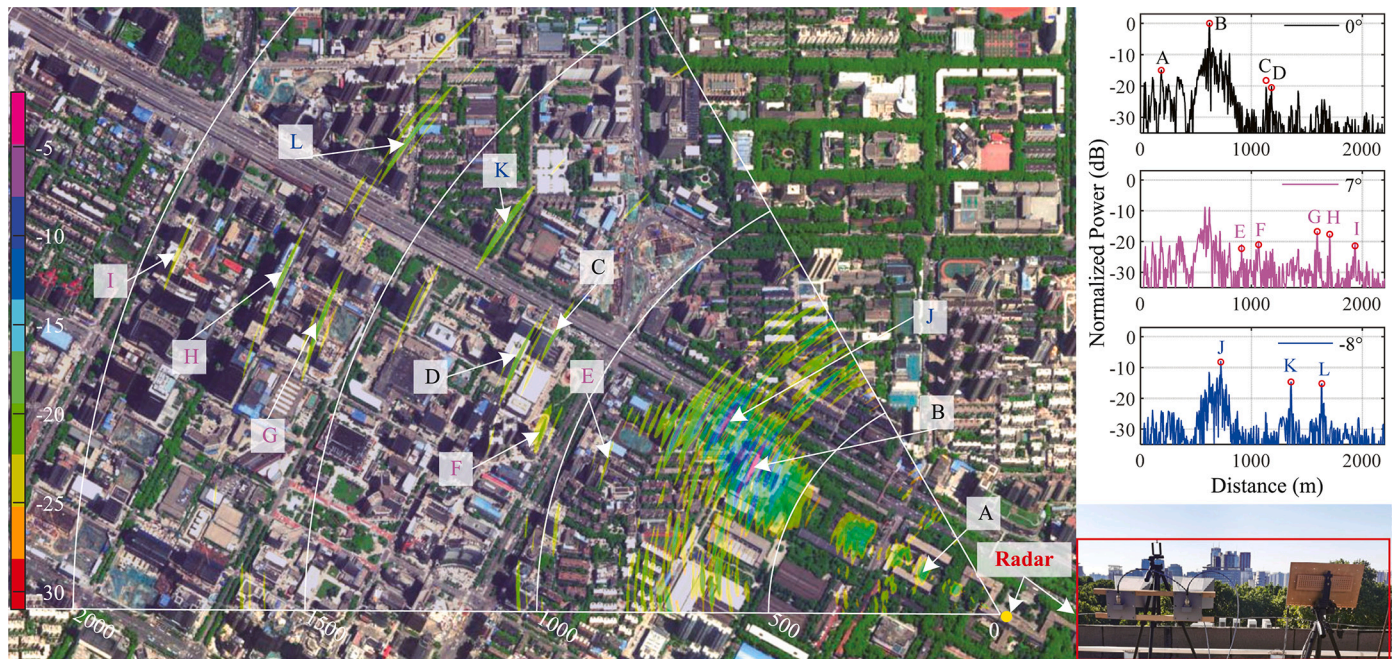
Fig. 7. A two-dimensional space-distance radar imaging using the proposed FH-MIMO DFRC waveform and the hardware platform built in Section 4.1. The zero-Doppler channel is observed, and hence only static targets are shown in the radar imaging. Representative targets are pinpointed based on the latest satellite map of the location [39]. The distance profiles of three angles covering most pinpointed targets are separately plotted in the upper-right sub-figure. The lower-right sub-figure is a trimmed version of Fig. 2, giving a glimpse of the radar platform and the surrounding environment.

cated by 'N'). Different modulation schemes and settings are simulated, where 8 or 16 in the figure denotes the PSK modulation order and 0.5 or 1 denotes the hop duration (in microseconds). Based on (23), the total data rates are 0.975 Mbps and 1.125 Mbps, respectively, for curves with labels ending by 8 and 16. From Fig. 6, we can see that the proposed method, which estimates and compensates for all hardware errors, outperforms the benchmark method, which ignores the carrier frequency offset and the hardware differences between the different receiving channels. The comparison also illustrates the effectiveness of the proposed designs and methods for estimating channel and hardware imperfections.

In addition, from Fig. 6, we can see that FHCS generally has lower SER than PSK modulations. This is consistent with previous work, such as [18]. We also see that when the hop duration doubles, both FHCS and PSK achieve better SER performance. This is because the demodulation SNR increases with the hop duration. For FHCS, we can see from Fig. 6 that the modulation order does not affect its SER performance. This is due to the way FHCS is demodulated. In particular, as shown in Section 2.2, we only need to identify DFT peaks to demodulate FHCS, where the phases of the peaks are irrelevant.

From Fig. 6, we can see that the traditional method shows interesting intersections between curves under the same PSK modulation but with different hop durations. In contrast, the proposed method does not have this anti-intuition result. This is because the benchmark method [33] ignores the CFO, while we do not. In particular, in the presence of CFO, the carrier phase error accumulates over time and becomes more dominant when the hop duration is large; see (6). When SNR is low, a large T helps improve the communication SNR. However, when the SNR is high, the phase error caused by CFO dominates the overall degradation of communication performance.

4.3. Experimental results

Using the hardware platforms presented in Section 4.1, we perform over-the-air experiments. As shown in Fig. 2, the radar transceiver is placed on top of a building with a height of about 20 m. Fig. 7 plots the radar imaging results, where the observation distance is up to 3 km

from the radar and the angular range is $[-30°, 30°]$ around the normal direction of the radar. To plot the 2D radar imaging, the zeroth Doppler channel of the MTD result, as obtained in (20), is extracted in each CPI. Then, the beamforming, as shown in (18), is performed to scan the angular range with a step of 1°.

To calibrate the radar transceiver arrays, we use a known target (i.e., target B in Fig. 7) to calculate the array calibration coefficients, i.e., $\mathbf{e}_r \otimes \mathbf{e}_t$ given in (22). In particular, we place the radar transceiver so that target B is in the normal direction of the radar. Since the target range is known, we extract the signal of the p-th ($p = 0, 1, \cdots, P-1$) virtual spatial channel, i.e., the signal given in (20), at the known range and the Doppler bin. Given the radar configuration in Table 2, we have $P(= 24)$ virtual channels. Ideally, the extracted signals should be the same. However, since they are affected by the array calibration errors, their values may be different. Therefore, we use the signal of the first virtual spatial channel as a reference, and all other extracted signals are normalized to the reference signal, resulting in the array calibration vector. In fact, in our experiment, we do not have the facilities to calibrate the radar transceiver arrays. Using the anchor-based method described above, we are able to obtain a relatively well-calibrated array, as shown by the high agreement between the measured and mapped targets in Fig. 7.

In the figure, we superimpose the radar image over a satellite map of the observed area, where the map is obtained from [39]. From Fig. 7, we can see that the strong signals in the radar image correspond well to the objects observed on the map. The distance profiles at the three selected angles further highlight the most accurately located targets. This illustrates the effectiveness of the array calibration described above. Even more importantly, it confirms that the proposed waveform modifications for FH-MIMO radar to accommodate data communications do not appear to affect the primary radar function.

Next, we illustrate the performance of communications. In the first set of experiments (i.e., Figs. 7, 8 and 9), we place the communication receiver, shown in Fig. 3, approximately ten meters behind the radar transmitter antennas (which are placed outdoors as shown in Fig. 2). That is, the communication receiver is in the Line-of-Sight (LoS) posterior views of radar transmitter antennas. The proposed communication

(a)   (b)
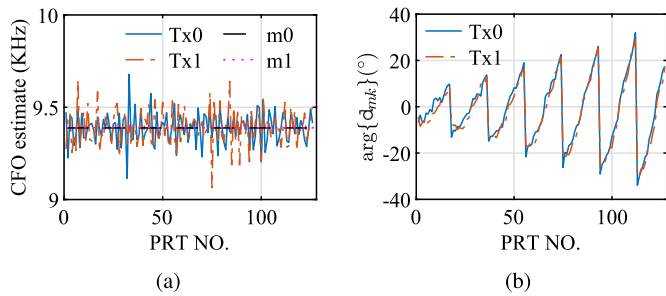
Fig. 8. The CFO estimate, i.e., $\widehat{\Delta\omega}$, is illustrated in (a); the estimate of $\arg\{\mathsf{d}_{mk}\}$ in (b), where $\widehat{\Delta\omega}$ is obtained in (11) and d_{mk} in (14). Note that m0 and m1 are the average of Tx0 and Tx1, respectively. In a CPI, the value of k cyclic increases with the PRTs, and it can be known from (14) that for a k, $\arg\{\mathsf{d}_{mk}\}$ increases with the PRT index.

(a)   (b)   (c)

(d)   (e)   (f)
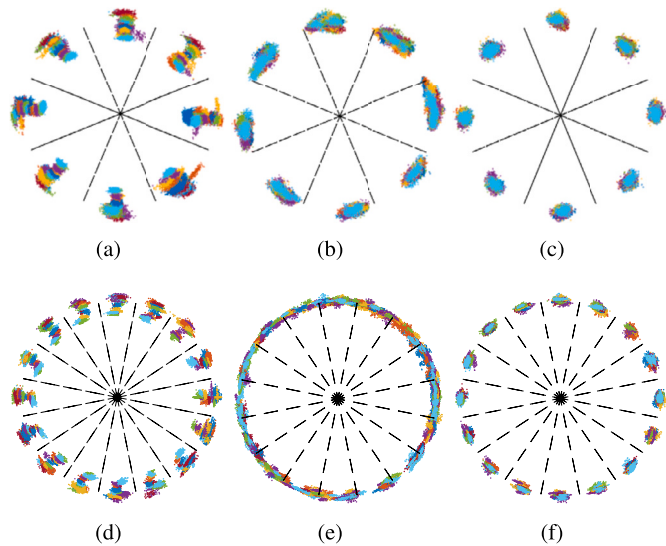
Fig. 9. Illustrating of the demodulation performance, where the top row is for 8PSK, the second row is for 16PSK, and the gain of the communication receiver is set to 36 dB. In the first column, we simulate the previous method [19] with CFO compensated but without considering frequency-dependent transceiver gains. In the second column, the latter are compensated for the previous method [19], but the CFO is not. While neither is considered by the previous method, we try to show the individual effects of the two factors. The third column is based on the proposed design in Section 3.

demodulation method, as summarized in Algorithm 1, is performed on the collected experimental data.

Fig. 8(a) plots the CFO estimate obtained for each pair of two consecutive PRTs; see (11), since there are 128 PRTs, there are 127 results. We see that there is a non-negligible CFO between the radar transmitter and the communication receiver. We also see that the two communication receivers have different CFOs. In addition, we see that the CFO estimate changes with time but remains around approximately a fixed value (m0 and m1 in Fig. 8(a)). The CFOs of the two channels should be the same. However, the CFO estimation in our scheme is based on noisy signals captured in each radar PRT. Thus, the slight fluctuation in the CFO estimates is caused by the unavoidable noise in the signals. As seen in Fig. 8(a), the CFO estimates remain very close to the average results, as indicated by m0 and m1. This validates the slowly varying nature of the CFO in a given coherent processing period. This also confirms that we can average the estimates of the CFO over a suitable time period to obtain a more accurate estimation. Fig. 8(b) plots the estimate of $\arg\{\mathsf{d}_{mk}\}$. We can see that $\arg\{\mathsf{d}_{mk}\}$ changes over PRTs in the way depicted by (14). Recall that, in the proposed waveform design, the i-th PRT estimates d_{mk} for $k = (i)_{K-1}$, where $()_{K-1}$ denotes modulo-$(K-1)$.

Fig. 10. Indoor SER Test Scenario.
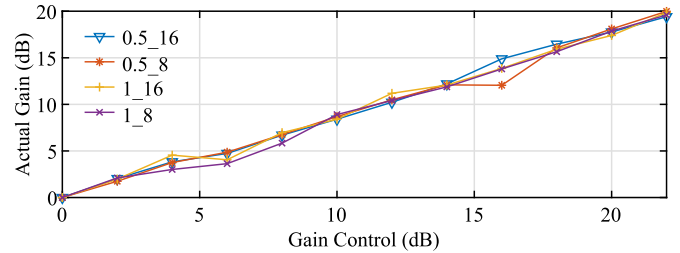
Fig. 11. Actual gain versus receive gain.

Fig. 9 shows the scatter plots of the demodulated communication symbols, where 8PSK is given in the first row, and 16PSK is in the second row. The first two columns are the results obtained by the previous method [19], while the proposed design achieves the last one. In addition, the effects of CFO and frequency-dependent transceiver gains are observed in the first and second columns, respectively. We see that, without considering the two practical factors, the error radii of constellation points decoded by the previous method are much larger than those under the proposed design. Moreover, we also see that the transceiver gains, whose effects are shown in Fig. 9(e), have a more severe impact on the communication performances than the CFO, as observed in Fig. 9(d). The proposed design takes into account the practically unavoidable hardware errors, thus significantly reducing the error radii of the constellation points.

In the second set of experiments to validate the communication performance, we observe the SER performance under different SNRs, as simulated in Fig. 6. To precisely control demodulation SNRs, we use two SDRs indoors, one transmitting and one receiving, as illustrated in Fig. 10. The transmitting SDR is the one used for radar transmitter but is equipped with two omnidirectional antennas (with 12 dBi). During the experiment, we set the gains of the two transmitting RF chains as 0 dB and adjust the gains of the receiving RF chains to achieve different demodulation SNRs. Fig. 11 plots the actual gain under different gain control. The actual gain is estimated by averaging the power of the received signal which is normalized to the estimated gain under the 0 dB gain control. Note that changing the gain may also incur changes to the receiver noise level. Therefore, the receiver gain is an approximation of the true SNR.

Fig. 12 compares the SER performance of the benchmark and proposed methods based on experimental data, where 800 CPIs are collected, corresponding to $1,024,000$ demodulation results. Using the same configurations as in Fig. 6, the total data rates are 0.975Mbps and 1.125Mbps, for curves with labels ending by 8 and 16, respectively. We can see that the proposed design and methods can lead to non-trivial improvements in SER performance over the prior art. We also see that the trends of all SER curves match well with what was observed in Fig. 6. This validates the proposed design is capable of compensating for practical hardware imperfections. The curves in Fig. 12 are not as smooth as the simulated curves in Fig. 6. This is partly because the gain control curve is not ideally linear and stable during the collection of four sets of data, as shown in Fig. 11. This may also be due to the fact that the receiver gain, as adjusted during experiments, is an approximation of the actual SNR.
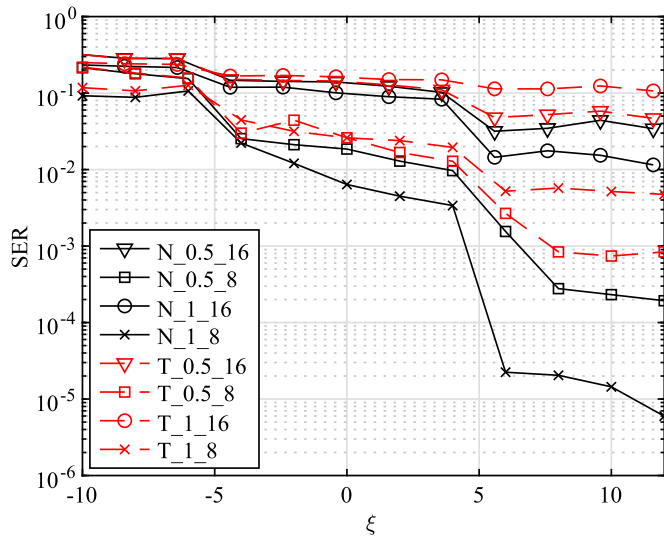
Fig. 12. Experimental SER versus ξ, where ξ is the difference between the receiver gain and the number of bits per symbol in decibels. In the legend, 'N' denotes 'the proposed new method', while 'T' represents the 'traditional method' [19]; 0.5 and 1 are different hop duration in milliseconds; and 8 and 16 are the modulation orders of PSK symbols.

5. Conclusion

In this work, a practical FH-MIMO DFRC is developed that comprehensively treats all practically unavoidable hardware errors, including STO, CFO, and front-end imperfections of transceivers. We model these errors and analyze their effects on the FH-MIMO DFRC. Furthermore, we design new waveforms and develop a low-complexity algorithm that jointly estimates all hardware errors at a communication receiver. In addition, we build an FH-MIMO JRC experimental platform using low-cost SDR and COST products that are popular in IoT system designs. Outdoor and indoor experiments are conducted using the platform. By applying the proposed designs to the collected experimental data, high performance is achieved for both radar and communication.

CRediT authorship contribution statement

Jiangtao Liu: Data curation, Formal analysis, Investigation, Methodology, Validation, Writing – original draft. **Kai Wu:** Conceptualization, Formal analysis, Investigation, Methodology, Supervision, Writing – review & editing. **Tao Su:** Funding acquisition, Investigation, Project administration, Resources, Supervision, Writing – review & editing. **J. Andrew Zhang:** Investigation, Methodology, Resources, Supervision, Writing – review & editing.

Declaration of competing interest

The authors declare that they have no known competing financial interests or personal relationships that could have appeared to influence the work reported in this paper.

Appendix A. Illustrating $|\Delta\omega N_{\mathrm{p}}\Delta T_s| \ll \frac{2\pi}{2^J}$

We note that $|\Delta\omega N_{\mathrm{p}}\Delta T_s| = 2\pi\rho f_c \cdot f_s T_{\mathrm{p}} \cdot \rho T_s^{\mathrm{t}} = 2\pi\rho^2 T_{\mathrm{p}} f_c$. Thus, to have the inequality in the appendix title satisfied, we only need to show $2\pi\rho^2 T_{\mathrm{p}} f_c \ll \frac{2\pi}{2^J}$. This is essentially an inequality of T_{p}, i.e., $T_{\mathrm{p}} \ll \frac{1}{2^J\rho^2 f_c}$. We note that this last inequality is practically legitimate. For example, by setting $f_s^{\mathrm{t}} = 40$ MHz, $f_c = 5.5$ GHz, $\rho = 10$ ppm, and $2^J = 16$, we have $\frac{1}{2^J\rho^2 f_c} = 0.1136$ s. We note that T_{p} is generally far less than 0.1136 s, such as $T_{\mathrm{p}} = 40$ μs used in our experiments.

References

[1] Y. Cui, F. Liu, X. Jing, J. Mu, Integrating sensing and communications for ubiquitous IoT: applications, trends, and challenges, IEEE Netw. 35 (5) (2021) 158–167.

[2] F. Liu, C. Masouros, A.P. Petropulu, H. Griffiths, L. Hanzo, Joint radar and communication design: applications, state-of-the-art, and the road ahead, IEEE Trans. Commun. 68 (6) (2020) 3834–3862.

[3] J.A. Zhang, M.L. Rahman, K. Wu, X. Huang, Y.J. Guo, S. Chen, J. Yuan, Enabling joint communication and radar sensing in mobile networks—a survey, IEEE Commun. Surv. Tutor. 24 (1) (2022) 306–345.

[4] K. Wu, J.A. Zhang, X. Huang, Y.J. Guo, Frequency-hopping MIMO radar-based communications: an overview, IEEE Aerosp. Electron. Syst. Mag. 37 (4) (2022) 42–54.

[5] A. Hassanien, M.G. Amin, E. Aboutanios, B. Himed, Dual-function radar communication systems: a solution to the spectrum congestion problem, IEEE Signal Process. Mag. 36 (5) (2019) 115–126.

[6] M. Roberton, E. Brown, Integrated radar and communications based on chirped spread-spectrum techniques, in: IEEE MTT-S International Microwave Symposium Digest, 2003, Vol. 1, 2003, pp. 611–614.

[7] G.N. Saddik, R.S. Singh, E.R. Brown, Ultra-wideband multifunctional communications/radar system, IEEE Trans. Microw. Theory Tech. 55 (7) (2007) 1431–1437.

[8] P. Barrenechea, F. Elferink, J. Janssen, FMCW radar with broadband communication capability, in: 2007 European Radar Conf., IEEE, 2007, pp. 130–133.

[9] A. Hassanien, M.G. Amin, Y.D. Zhang, F. Ahmad, Dual-function radar-communications: information embedding using sidelobe control and waveform diversity, IEEE Trans. Signal Process. 64 (8) (2016) 2168–2181.

[10] X. Wang, A. Hassanien, M.G. Amin, Dual-function MIMO radar communications system design via sparse array optimization, IEEE Trans. Aerosp. Electron. Syst. 55 (3) (2019) 1213–1226.

[11] T.W. Tedesso, R. Romero, Code shift keying based joint radar and communications for EMCON applications, Digit. Signal Process. 80 (2018) 48–56.

[12] A. Hassanien, E. Aboutanios, M.G. Amin, G.A. Fabrizio, A dual-function MIMO radar-communication system via waveform permutation, Digit. Signal Process. 83 (2018) 118–128.

[13] A. Hassanien, B. Himed, B.D. Rigling, A dual-function MIMO radar-communications system using frequency-hopping waveforms, in: 2017 IEEE Radar Conference (RadarConf), 2017, pp. 1721–1725.

[14] I.P. Eedara, A. Hassanien, M.G. Amin, B.D. Rigling, Ambiguity function analysis for dual-function radar communications using PSK signaling, in: 52nd Asilomar Conf. Signals, Syst., and Computers, 2018, pp. 900–904.

[15] I.P. Eedara, M.G. Amin, Dual function FH MIMO radar system with DPSK signal embedding, in: 2019 27th European Signal Process. Conf. (EUSIPCO), 2019, pp. 1–5.

[16] I.P. Eedara, M.G. Amin, A. Hassanien, Analysis of communication symbol embedding in FH MIMO radar platforms, in: 2019 IEEE Radar Conf. (RadarConf), 2019, pp. 1–6.

[17] W. Baxter, E. Aboutanios, A. Hassanien, Dual-function MIMO radar-communications via frequency-hopping code selection, in: 2018 52nd Asilomar Conf. on Signals, Syst., and Computers, 2018, pp. 1126–1130.

[18] K. Wu, Y.J. Guo, X. Huang, R.W. Heath, Accurate channel estimation for frequency-hopping dual-function radar communications, in: 2020 IEEE International Conference on Communications Workshops (ICC Workshops), 2020, pp. 1–6.

[19] K. Wu, J.A. Zhang, X. Huang, Y.J. Guo, R.W. Heath, Waveform design and accurate channel estimation for frequency-hopping MIMO radar-based communications, IEEE Trans. Commun. 69 (2) (2021) 1244–1258.

[20] K. Wu, J.A. Zhang, X. Huang, Y.J. Guo, J. Yuan, Reliable frequency-hopping MIMO radar-based communications with multi-antenna receiver, IEEE Trans. Commun. 69 (8) (2021) 5502–5513.

[21] K. Wu, J. Andrew Zhang, X. Huang, Y. Jay Guo, Integrating secure communications into frequency hopping MIMO radar with improved data rate, IEEE Trans. Wirel. Commun. 21 (7) (2022) 5392–5405.

[22] MathWorks, User guide (R2021a), https://www.mathworks.com/help/pdf_doc/supportpkg/xilinxzynqbasedradio/xilinxzynqbasedradio_ug.pdf. (Accessed 2 October 2022).

[23] ADI, User guide (04 Nov 2021), https://wiki.analog.com/resources/eval/user-guides/ad-fmcomms3-ebz. (Accessed 2 October 2022).

[24] D.M. Wong, B.K. Chalise, J. Metcalf, M. Amin, Information decoding and SDR implementation of DFRC systems without training signals, in: ICASSP 2021, 2021, pp. 8218–8222.

[25] D. Ma, N. Shlezinger, T. Huang, Y. Shavit, M. Namer, Y. Liu, Y.C. Eldar, Spatial modulation for joint radar-communications systems: design, analysis, and hardware prototype, IEEE Trans. Veh. Technol. 70 (3) (2021) 2283–2298.

[26] P. Kumari, A. Mezghani, R.W. Heath, JCR70: a low-complexity millimeter-wave proof-of-concept platform for a fully-digital SIMO joint communication-radar, IEEE Veh. Technol. Mag. 2 (2021) 218–234.

[27] Y. Liu, Z. Du, F. Zhang, Z. Zhang, W. Yu, Implementation of radar-communication system based on GNU-Radio and USRP, in: 2019 ComComAp, 2019, pp. 417–421.

[28] L.C. Tran, D.T. Nguyen, F. Safaei, P.J. Vial, An experimental study of OFDM in software defined radio systems using GNU platform and USRP2 devices, in: International Conference on ATC 2014, 2014, pp. 657–662.

[29] C.W. Rossler, E. Ertin, R.L. Moses, A software defined radar system for joint communication and sensing, in: 2011 IEEE RadarCon (RADAR), 2011, pp. 1050–1055.

[30] W.A.H.M.A. Richards, J. Scheer, W.L. Melvin, Principles of Modern Radar, 2010.

[31] MathWorks, CFAR detection, http://www.bom.gov.au/australia/radar/info/nsw_info.shtml, 2021. (Accessed 2 October 2022).

[32] R. Schmidt, Multiple emitter location and signal parameter estimation, IEEE Trans. Antennas Propag. 34 (3) (1986) 276–280.

[33] K. Wu, J.A. Zhang, X. Huang, Y.J. Guo, Accurate frequency estimation with fewer dft interpolations based on Padé approximation, IEEE Trans. Veh. Technol. 70 (7) (2021) 7267–7271.

[34] Xilinx, User guide (UG954 (v1.8) August 6, 2019), https://www.xilinx.com/support/documentation/boards_and_kits/zc706/ug954-zc706-eval-board-xc7z045-ap-soc.pdf. (Accessed 2 October 2022).

[35] AVNET, User guide (version 1.1 August 1st, 2012), https://www.avnet.com/wps/portal/us/products/avnet-boards/avnet-board-families/zedboard. (Accessed 2 October 2022).

[36] Epson, Data sheet, https://www5.epsondevice.com/en/products/crystal_unit/tsx3225.html. (Accessed 2 October 2022).

[37] ADI, User guide, https://www.analog.com/media/en/technical-documentation/data-sheets/AD9361.pdf. (Accessed 2 October 2022).

[38] S. Rao, Tdm mimo radar, https://www.ti.com/lit/an/swra554a/swra554a.pdf, 2018. (Accessed 2 October 2022).

[39] GaoDe, Map, https://ditu.amap.com/. (Accessed 2 October 2022).